IEEE Access
Multidisciplinary | Rapid Review | Open Access Journal

Received October 22, 2019, accepted November 1, 2019, date of publication November 4, 2019, date of current version November 15, 2019.

Digital Object Identifier 10.1109/ACCESS.2019.2951537

Accurate Ultra-Wideband Array Radar Imaging Using Four-Dimensional Unitary ESPRIT

KAZUSHI MORIMOTO[1], TAKUYA SAKAMOTO[2,3], (Senior Member, IEEE), AND TORU SATO[4], (Member, IEEE)

[1]MaRI Company, Ltd., Kyoto 600-8815, Japan
[2]Graduate School of Engineering, Kyoto University, Kyoto 615-8510, Japan
[3]Japan Science and Technology Agency, Saitama 332-0012, Japan
[4]Institute for Liberal Arts and Sciences, Kyoto University, Kyoto 606-8501, Japan

Corresponding author: Takuya Sakamoto (sakamoto.takuya.8n@kyoto-u.ac.jp)

This work was supported in part by the Japan Society for the Promotion of Science (JSPS) KAKENHI under Grant 15K18077, Grant 15KK0243, and Grant 19H02155, in part by the Japan Science and Technology Agency promote individual research to nurture the seeds of future innovation and organize unique, innovative network (PRESTO) under Grant JPMJPR1873, and in part by the Japan Science and Technology Agency (JST) Center of Innovation (COI) Program under Grant JPMJCE1307.

ABSTRACT Adaptive signal processing techniques can estimate the directions of arrival (DOAs), ranges, and radial velocities of radar targets with high resolution when applied in the space, frequency, and time domains, respectively. However, the performance of these techniques is limited when they are applied separately in each domain. Recently, adaptive signal processing algorithms based on high-dimensional signal subspaces have been studied extensively. We apply a four-dimensional unitary estimation of signal parameters via rotational invariant techniques (ESPRIT) algorithm for the simultaneous estimation of the DOAs, ranges, and Doppler velocities of multiple targets in an ultra-wideband radar imaging setting and show the effectiveness of the high-dimensional ESPRIT for the near-field imaging of distributed moving targets. The four-dimensional ESPRIT algorithm is demonstrated to be able to separate targets moving in close proximity, whereas the two- and three-dimensional ESPRIT algorithms fail to separate these targets accurately because of their limited resolutions. The application of the high-dimensional ESPRIT to near-field radar imaging covers a wide range of applications that require the measurement of multiple moving targets in close proximity. An example of such an application is radar-based human monitoring. Therefore, the superior resolution of the high-dimensional ESPRIT has the potential to improve the performance of various real-world security and healthcare systems.

INDEX TERMS Adaptive signal processing, direction-of-arrival, multidimensional signal processing, radar imaging, ultra wideband radar.

I. INTRODUCTION

Recently, radar-based monitoring of human activities has been attracting increasing attention, particularly for use in healthcare and security applications. Unlike camera-based monitoring techniques, radar-based techniques can avoid privacy concerns. Additionally, radar-based systems can measure people through various materials (e.g., building walls, clothing, and bed sheets) and are not affected by lighting conditions. In particular, ultra-wideband (UWB) radar is considered to be promising because it provides high-range resolution that enables near-field imaging.

One of the most popular radar-based techniques for monitoring human activities is based on micro-Doppler, which is a time-dependent Doppler shift caused by limb motion and obtained through time-frequency analysis. Because this approach requires only a Doppler shift as a function of time, the system does not require antenna arrays or wideband signals. Therefore, the measurement can be implemented using a relatively low-cost system, which has attracted a number of research groups [1]–[9].

In addition to the Doppler shift, range information can be also used if wideband signals are used. The range-frequency domain expression is also called an inverse synthetic aperture radar (ISAR) image, which exhibits a large amount of information on human activities [10]–[12]. The use of three-dimensional (3D) time-range-frequency domain

The associate editor coordinating the review of this manuscript and approving it for publication was Liangtian Wan.

analysis [13] has also been reported for monitoring human activities.

By introducing multiple antenna elements, spatial resolution can be obtained, realizing human body imaging. Lin and Ling [14], [15] developed a frequency-domain interferometry technique that separates echoes in the frequency domain using their different Doppler shifts, and estimates the directions of arrival (DOAs) using three antenna elements. Their studies were followed by other research groups [16]–[19]. Because these studies use the Fourier transform to separate multiple echoes in the frequency domain, the echoes cannot be separated if their Doppler velocities happen to be the same. To resolve this issue, frequency-domain interferometry was combined with subspace-based algorithms [20], [21]. However, these algorithms perform signal filtering separately in multiple domains; first in the frequency domain to estimate the Doppler velocities and then in the spatial domain to estimate the DOAs, and this compromises both the spatial and frequency resolutions.

In radar signal processing, space-time adaptive processing (STAP) [22], [23] has been studied mainly for far-field targets. In STAP, multidimensional adaptive signal processing is performed simultaneously in the space-time domain. STAP has been shown to be effective for separating multiple radar echoes with high resolution. Conventionally, most STAP approaches are based on the Capon method [24] that is a well-known classic algorithm used to achieve high resolution. The Capon method, however, suffers from a heavy computational burden and limited resolution. Additionally, the exact response of each antenna element must be calibrated in advance, which makes Capon-based STAP difficult to use in practice.

By contrast, the estimation of signal parameters via rotational invariant techniques (ESPRIT) algorithm achieves a higher resolution with a less computational cost because a time-consuming peak search is not necessary. Additionally, ESPRIT does not require information about antenna element responses. Multidimensional ESPRIT algorithms have been intensively studied: Haardt and Nossek [25] applied a 3D ESPRIT algorithm in the space-time domain to estimate two DOAs and a Doppler frequency. Multidimensional ESPRIT has also been proposed for use in wireless communications [26], [27]. Sakaguchi *et al.* [26] applied the 3D ESPRIT algorithm in the space-frequency domain to estimate two DOAs and the time of arrival (TOA). A four-dimensional (4D) ESPRIT algorithm was applied in the space-time-frequency domain [27] and two DOAs, the TOA, and the Doppler frequency were successfully estimated using this algorithm. Haardt *et al.* [28] also developed a parameter estimation technique using a high-order singular value decomposition (SVD), and Raimondi *et al.* [29] and Sahnoun *et al.* [30] proposed a multidimensional ESPRIT algorithm based on tensor decomposition. These studies mostly focused on the application of the multidimensional ESPRIT algorithm to wireless communications and far-field target detection using radar. Literature on the use of multidimensional ESPRIT for UWB radar near-field imaging is still scarce, particularly for distributed targets, such as the human body. It is still unclear how much performance improvement can be achieved using multidimensional ESPRIT applied to near-field UWB radar imaging, which is related to recent active research on the noncontact measurement of human activities and patient monitoring.

In this paper, we demonstrate the imaging performance of multiple moving targets located in close proximity using UWB radar and the 4D unitary ESPRIT algorithm in the space-time-frequency domain for the joint estimation of the DOAs (DOA_1 and DOA_2), Doppler velocity, and range. Additionally, to improve both the imaging resolution and imaging accuracy, we also introduce a new pairing algorithm to associate signals that are found in the different domains of multiple dimensions. We evaluate the performance of the 4D ESPRIT-based imaging algorithm using simulations and study its resolution quantitatively by comparing it with two other conventional methods: one that uses two-dimensional (2D) ESPRIT and another that uses 3D ESPRIT. Although recent theory-based research has been focused on tensor-based ESPRIT algorithms instead of matrix-based ESPRIT algorithm, we focus on matrix-based multidimensional ESPRIT. Note that recent studies in fast tensor-based approaches for DOA estimation have reported that they provide more accurate DOA estimation than matrix-based methods at the cost of lower complexity [31]. In future studies, we will consider using fast tensor-based approaches for near-field imaging.

The novel aspects of the present paper are as follows: (1) 4D unitary ESPRIT is applied for the first time to UWB radar imaging, assuming its application to the imaging of a human body; and (2) the near-field imaging accuracies of the 2D, 3D, and 4D unitary ESPRIT algorithms are compared to evaluate the importance of the high-dimensional unitary ESPRIT algorithm.

In this paper, we use the following notations: Lowercase a for scalars, uppercase A for matrices, and boldface lowercase $\boldsymbol{a}$ for vectors. Vectors are regarded as one-column matrices. The complex conjugate is denoted by a superscript asterisk a^*. The matrix transpose is denoted by a superscript T $\boldsymbol{a}^{\mathrm{T}}$ and A^{T}. The matrix conjugate transpose is denoted by a super script H. I_n is an $n \times n$ identity matrix. The symbols $\otimes$ and $\odot$ denote the Kronecker product and Khatri–Rao product, respectively. $\mathrm{Re}\{z\}$ and $\mathrm{Im}\{z\}$ denote the real and imaginary parts of complex number z, respectively, where z can be a scalar, vector or matrix. $\mathrm{diag}\{a(i)\}_{i=1}^{N}$ denotes an $N \times N$ diagonal matrix whose entries are all zero except for its main diagonal, where the diagonal entries starting in the upper left corner are $a(1), a(2), \cdots, a(N)$.

II. SYSTEM MODEL

A. ARRAY MODEL

In our system, the presence of L point-like targets is assumed, and these targets move within a half space, where $y > 0$ in the xyz coordinate system. The Doppler velocity and range of the

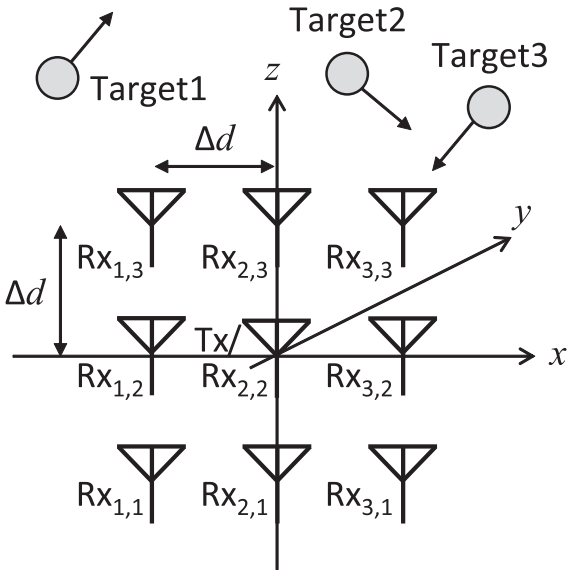

FIGURE 1. System model with a single transmitting element, 3 × 3 receiving elements, and three point targets.

$l(=1,\cdots,L)$-th target are denoted by v_l and r_l, respectively. The Doppler velocity is approximated as the radial velocity from the transmitting antenna (located at the coordinate origin). The DOAs of the l-th target from the z-y and x-y planes are θ_{l1} and θ_{l2}, respectively.

A single transmitting element Tx and $M_1 \times M_2$ receiving elements $\mathrm{Rx}_{1,1},\cdots,\mathrm{Rx}_{1,\mathrm{M}_2},\mathrm{Rx}_{2,1},\cdots,\mathrm{Rx}_{\mathrm{M}_1,\mathrm{M}_2}$ form a uniform rectangular planar array. All elements of the array are located on the x-z plane, where $y = 0$. The antenna elements are all assumed to have the same omnidirectional beam pattern. All errors caused by sensor imperfections, such as the mutual coupling error, gain-phase error, and position error, are all assumed to be negligible. Fig. 1 shows an example of the system model for $M_1 = 3$, $M_2 = 3$, and $L = 3$. As shown in Fig. 1, a single transmitting element is located at the origin, whereas the receiving elements are located with a spacing of Δd in the x and z directions and form a rectangular planar array that is centered at the origin.

The radar system transmits UWB signals at a center frequency of f_c with a 3 dB bandwidth W from transmitting element Tx; the reflected echoes are then received by the receiving antenna elements $\mathrm{Rx}_{i,j}$ and sampled with a slow-time interval of Δt and fast-time interval of $\Delta\tau$, which corresponds to the range sampling interval $\Delta r = c\Delta\tau/2$, where c is the speed of light. For simplicity, both multipath and multiple scattering effects are neglected in this paper.

B. SIGNAL MODEL

We assume that all received echoes have the same known waveform. The received signals are sampled in terms of both slow time and fast time, and the signals are then Fourier transformed with respect to fast time. The signals are thus expressed using slow time $0 \le t \le T$ and fast frequency $f_c - W/2 \le f \le f_c + W/2$, where T is the observation time, f_c is the carrier frequency, and W is the bandwidth.

The signal received using antenna Rx_{m_1,m_2} is denoted by x'_{m_1,m_2,m_3,m_4} for slow time $t = m_3\Delta t$ and fast frequency $f = m_4\Delta f$. The indices m_1, m_2, m_3, m_4 are integers that range up to M_1, M_2, M_3, M_4, respectively; hence $m_i = 1, 2, \cdots, M_i$ for $i = 1, 2, 3, 4$.

The number of antenna elements M_1M_2 is determined by the antenna array, whereas the number of slow-time and fast-frequency samples are $M_3 = T/\Delta t$ and $M_4 = W/\Delta f$, where Δt and Δf are sampling intervals of slow time and fast frequency, respectively.

A signal sample denoted by x'_{m_1,m_2,m_3,m_4} corresponds to the antenna location $(x, z) = (\{m_1-(M_1+1)/2\}\Delta d, \{m_2-(M_2+1)/2\}\Delta d)$, slow time $m_3\Delta t$, and fast frequency $f = f_c+\{m_4-(M_4+1)/2\}\Delta f$, and is expressed as

$$x'_{m_1,m_2,m_3,m_4} = \sum_{l=1}^{L} s_l \prod_{i=1}^{4} \mathrm{e}^{\mathrm{j}\{m_i-[(M_i+1)/2]\}\mu_i(l)} + n'_{m_1,m_2,m_3,m_4}, \tag{1}$$

$$\begin{cases} \mu_1(l) = 2\pi f_c \cdot \Delta d \sin(\theta_{l1})/c, \\ \mu_2(l) = 2\pi f_c \cdot \Delta d \sin(\theta_{l2})/c, \\ \mu_3(l) = 2\pi f_c \cdot 2v_l\Delta t/c, \\ \mu_4(l) = 2\pi\,\Delta f \cdot 2r_l/c, \end{cases} \tag{2}$$

where $\mu_i(l)$ is an unknown parameter of the l-th target in dimension $i(=1, 2, 3, 4)$, s_l is the complex-valued amplitude of the l-th target, and n'_{m_1,m_2,m_3,m_4} is additive white Gaussian noise.

Because we assume that all echoes have the same known waveform, the received signal can be modeled as a superposition of multiple amplified and time-shifted template waveforms, and thus means that the template waveform $S_{\mathrm{ref}}(f)$ in the frequency domain can be measured in advance. To measure $S_{\mathrm{ref}}(f)$, an echo waveform from a known target (such as a reflector) located at a known position has to be measured prior to the actual measurement of the unknown targets. The measurement of $S_{\mathrm{ref}}(f)$ is called the calibration stage in the present paper. Using this template waveform measured in the calibration stage, we can perform whitening processing to compensate for the frequency-dependent response using a Wiener filter $W(m_4, \eta)$ expressed as

$$W(m_4, \eta) = \frac{S^*_{\mathrm{ref}}(f_c + \{m_4 - (M_4+1)/2\}\Delta f)}{|S_{\mathrm{ref}}(f_c + \{m_4 - (M_4+1)/2\}\Delta f)|^2 + \eta}. \tag{3}$$

By applying $W(m_4, \eta)$, we obtain x_{m_1,m_2,m_3,m_4} as

$$x_{m_1,m_2,m_3,m_4} = W(m_4, \eta)x'_{m_1,m_2,m_3,m_4}, \tag{4}$$

where η is a parameter related to the signal-to-noise ratio (SNR). After the filtering, the additive noise is white in the time (m_3) and space domains (m_1 and m_2), but is not white in the frequency domain (m_4). We set $\eta = 0$ throughout this paper, which corresponds to an inverse filter. As explained in Section IV-A, the transmitted and received signals both have a known Gaussian waveform, where the frequency-dependent radar cross section is not considered for simplicity.

As stated above, the proposed method requires a calibration stage prior to the actual measurement. Therefore, the proposed method is not a generalized method; some information about the environment must be known in advance to accomplish the calibration task.

III. UWB DOPPLER RADAR IMAGING ALGORITHM WITH 4D UNITARY ESPRIT

A. 4D UNITARY ESPRIT

In this section, we show how the Doppler velocity, range, and two DOAs (DOA_1 and DOA_2) can be estimated simultaneously using the 4D unitary ESPRIT algorithm in the time-space-frequency domain. Although the algorithm described below corresponds to a special case ($R = 4$) of the R-D unitary ESPRIT algorithm proposed by Haardt and Nossek [25], the exact procedures are restated here for convenience.

First, we define the unified signal vector $\boldsymbol{x}$ using x_{m_1,m_2,m_3,m_4} as

$$\boldsymbol{x} = \begin{bmatrix} x_{1,1,1,1} \\ x_{2,1,1,1} \\ \vdots \\ x_{M_1,1,1,1} \\ x_{1,2,1,1} \\ \vdots \\ x_{M_1,M_2,1,1} \\ x_{1,1,2,1} \\ \vdots \\ x_{M_1,M_2,M_3,1} \\ x_{1,1,1,2} \\ \vdots \\ x_{M_1,M_2,M_3,M_4} \end{bmatrix}. \tag{5}$$

$\boldsymbol{x}$ can also be expressed as

$$\begin{aligned} \boldsymbol{x} &= A[s_1, \cdots, s_L]^{\mathrm{T}} + \boldsymbol{n}, \\ A &= A'_4 \odot A'_3 \odot A'_2 \odot A'_1, \\ A'_i &= [\boldsymbol{a}(\mu_i(1)), \cdots, \boldsymbol{a}(\mu_i(L))], \\ \boldsymbol{a}(\mu_i(l)) &= [\mathrm{e}^{\mathrm{j}\{-(M_i-1)/2\}\mu_i(l)}, \cdots, \mathrm{e}^{\mathrm{j}\{(M_i-1)/2\}\mu_i(l)}]^{\mathrm{T}}, \\ \boldsymbol{n} &= \left[n_{1,1,1,1}, \cdots, n_{M_1,M_2,M_3,M_4}\right]^{\mathrm{T}}, \end{aligned} \tag{6}$$

where $\odot$ is the Khatri-Rao product, $\boldsymbol{a}(\mu_i(l))$ is the steering vector, A'_i is the steering matrix for dimension i, A is the multidimensional steering matrix, and $\boldsymbol{n}$ is the noise vector.

Each column of the multidimensional steering matrix A is centro-symmetric. Therefore, A can be transformed into the real-valued steering matrix $D = {Q_M}^{\mathrm{T}} A$ using the unitary matrix Q_M ($M = M_1M_2M_3M_4$) [25]. For any even $M = 2n$ with any positive integer n, unitary matrix Q_M is then given by

$$Q_{2n} = \frac{1}{\sqrt{2}} \begin{bmatrix} I_n & \mathrm{j}I_n \\ \Pi_n & -\mathrm{j}\Pi_n \end{bmatrix}. \tag{7}$$

As stated above, A is transformed into a real-valued matrix using a unitary transformation, which improves computational efficiency compared with the original ESPRIT algorithm using a complex matrix.

For any odd $M = 2n + 1$, unitary matrix Q_M is given by

$$Q_{2n+1} = \frac{1}{\sqrt{2}} \begin{bmatrix} I_n & \boldsymbol{0} & \mathrm{j}I_n \\ \boldsymbol{0}^{\mathrm{T}} & \sqrt{2} & \boldsymbol{0}^{\mathrm{T}} \\ \Pi_n & \boldsymbol{0} & -\mathrm{j}\Pi_n \end{bmatrix}, \tag{8}$$

where I_n is an identity matrix of size n, and Π_n is the $n \times n$ anti-diagonal matrix, which is defined as

$$\Pi_n = \begin{bmatrix} & & 1 \\ & 1 & \\ \cdot & & \\ 1 & & \end{bmatrix}. \tag{9}$$

The real-valued steering matrix $D = {Q_M}^{\mathrm{T}} A$ satisfies the rotational invariance requirement for dimension $i = 1, 2, 3, 4$ as follows:

$$\mathrm{Re}\{K_{(i)}\} D \Omega_i = \mathrm{Im}\{K_{(i)}\} D, \tag{10}$$

$$\Omega_i = \mathrm{diag}\{\omega_i(l)\}_{l=1}^{L}, \tag{11}$$

$$\omega_i(l) = \tan(\mu_i(l)/2), \tag{12}$$

$$K_{(i)} = Q^H_{M(M_i-1)/M_i} J_{(i)2} Q_M, \tag{13}$$

$$J_{(1)2} = I_{M_4} \otimes I_{M_3} \otimes I_{M_2} \otimes J_2^{(M_1)}, \tag{14}$$

$$J_{(2)2} = I_{M_4} \otimes I_{M_3} \otimes J_2^{(M_2)} \otimes I_{M_1}, \tag{15}$$

$$J_{(3)2} = I_{M_4} \otimes J_2^{(M_3)} \otimes I_{M_2} \otimes I_{M_1}, \tag{16}$$

$$J_{(4)2} = J_2^{(M_4)} \otimes I_{M_3} \otimes I_{M_2} \otimes I_{M_1}, \tag{17}$$

$$J_2^{(M_i)} = \left[\boldsymbol{0}_{(M_i-1)\times 1} I_{M_i-1}\right], \tag{18}$$

where $\otimes$ is the Kronecker product. If Ω_i in Eq. (10) can be estimated, then the 4D estimation parameters $\mu_i(l)$ can also be estimated using Eqs. (11) and (12).

Next, we explain how Ω_i is estimated from the observed $\boldsymbol{x}$. Parameter estimation using ESPRIT does not work well if the signals from multiple targets are strongly correlated. Smoothing is known to be an easy and effective processing step for the suppression of signal correlation [25]. As shown in the Appendix, the $M_{\mathrm{sub}} \times M_{\mathrm{sub}}$ correlation matrix R_{xx} is obtained after the application of 4D smoothing. Please note that, as explained in Section II, before inverse filtering, the Gaussian-shaped echo spectrum is not flat in the frequency domain, whereas the noise spectrum is white; after inverse filtering, the echo spectrum becomes flat, whereas the noise becomes non-white. Despite this, the non-whiteness of the noise does not affect 4D unitary ESPRIT significantly because of the 4D smoothing procedure. In this 4D smoothing process, the non-white noise is averaged over different frequencies, which makes the non-white noise whiter to some extent, and thus, the non-whiteness of the raw noise sequence does not greatly affect the ESPRIT algorithm and resultant images.

The eigenvalue decomposition of correlation matrix R_{xx} allows L eigenvectors $\boldsymbol{v}_1, \cdots, \boldsymbol{v}_L$ that correspond

to the L largest eigenvalues to be extracted. Subspace span($\boldsymbol{v}_1, \cdots, \boldsymbol{v}_L$) coincides with an L-dimensional subspace that is spanned by L row vectors of D. Therefore, when the signal eigenvectors are defined as $E_s = [\boldsymbol{v}_1 \cdots \boldsymbol{v}_L]$, an $L \times L$ matrix T exists that satisfies $D = E_s T$. Substituting $D = E_s T$ into Eq. (10) yields

$$\mathrm{Re}\{K_{(i)}\}E_s \Upsilon_i = \mathrm{Im}\{K_{(i)}\}E_s, \tag{19}$$

$$\Upsilon_i = T\Omega_i T^{-1}, \tag{20}$$

where Υ_i is estimated by applying a total least squares algorithm [32] to Eq. (19). Diagonal matrix Ω_i is obtained using the eigenvalue decomposition that was applied to Υ_i.

B. ESTIMATION OF THE NUMBER OF TARGETS USING THE MINIMUM DESCRIPTION LENGTH

In the ESPRIT algorithm, the information about the number of targets L is required when extracting L signal eigenvectors $\boldsymbol{v}_1, \cdots, \boldsymbol{v}_L$ from the $M_{\mathrm{sub}}(\geq L)$ eigenvectors of the $M_{\mathrm{sub}} \times M_{\mathrm{sub}}$ matrix R_{xx}. We use the minimum description length (MDL) to estimate the number of targets. The MDL has often been used in (non-multidimensional) adaptive array processing to estimate the number of targets in combination with eigenvalue decomposition of the correlation matrix for DOA estimation [33], [34].

The MDL-based method used to estimate the number of targets L is explained below. If the correlation can be completely suppressed by smoothing, then eigenvalue λ_i of correlation matrix R_{xx}, which is arranged in descending order, satisfies

$$\lambda_1 \geq \cdots \geq \lambda_L > \lambda_{L+1} = \cdots = \lambda_{M_{\mathrm{sub}}} = \sigma^2, \tag{21}$$

where σ^2 is the noise power. Therefore, the number of targets L can be estimated by counting the number of eigenvalues that are larger than σ^2. However, because the number of smoothing operations N is actually finite, the (signal and noise) eigenvalues have fluctuations that depend on N and σ^2. To overcome this difficulty, the MDL-based method estimates the number of targets based on the information theoretic criteria used for model identification. Criterion MDL(l) that is used in this paper is given by

$$\mathrm{MDL}(l) = -\log\left\{\frac{\prod_{j=l+1}^{M_{\mathrm{sub}}}\lambda_j}{\left(\overline{\sigma^2}(l)\right)^{M_{\mathrm{sub}}-l}}\right\}^N + \frac{1}{2}l(2M_{\mathrm{sub}}-l)\log N, \tag{22}$$

$$\overline{\sigma^2}(l) = \frac{1}{M_{\mathrm{sub}}-l}\sum_{j=l+1}^{M_{\mathrm{sub}}}\lambda_j, \tag{23}$$

where the value of l that minimizes MDL(l) is used to calculate the estimated number of targets as $\hat{L} = \arg\min_l \mathrm{MDL}(l)$.

C. PAIRING EIGENVALUES IN MULTIDIMENSIONAL ESPRIT

1) OVERVIEW OF EXISTING EIGENVALUE PAIRING TECHNIQUES

As explained in the preceding sections, the 4D estimation parameters $\mu_i(l)$ are obtained independently for each dimension $i = 1, 2, 3, 4$ using Eqs. (11), (19), and (20). Hence, the ESPRIT procedure produces unpaired estimation parameters. Therefore, for L targets with four parameters (i.e., range, Doppler velocity, DOA$_1$, and DOA$_2$), there are $(L!)^3$ possible combinations. Thus, to achieve accurate imaging, it is necessary to determine the correct combinations among these possibilities.

In 2D ESPRIT, a simple automatic pairing method [35] is widely used. This method uses the fact that both Ω_i and Υ_i $i = 1, 2, 3, 4$ are real-valued. In this method, the eigenvalue decomposition of $\Upsilon_i + \mathrm{j}\Upsilon_j$ for $i, j \in \{1, 2, 3, 4\}$ is performed as follows:

$$\Upsilon_i + \mathrm{j}\Upsilon_j = T\left(\Omega_i^{(ij)} + \mathrm{j}\Omega_j^{(ij)}\right)T^{-1}, \tag{24}$$

$$\Omega_i^{(ij)} = \mathrm{diag}\left\{\omega_i^{(ij)}(l)\right\}_{l=1}^{L}, \tag{25}$$

$$\Omega_j^{(ij)} = \mathrm{diag}\left\{\omega_j^{(ij)}(l)\right\}_{l=1}^{L}, \tag{26}$$

where $\omega_i^{(ij)}(l)$ and $\omega_j^{(ij)}(l)$, which are the real and imaginary parts of the diagonal elements $\Omega_i^{(ij)} + \mathrm{j}\Omega_j^{(ij)}$, respectively, are the eigenvalues that are paired for the i-th and j-th domains for the l-th target.

However, this method is not applicable to 3D or higher-dimensional pairing. Simultaneous Schur decomposition (SSD) [25] is commonly used as a method for 3D or higher-dimensional pairing; however, SSD is known to suffer from high computational complexity because it requires iterative calculations. As an alternative, the chain pairing (CP) method [26] has been proposed for 3D or higher-dimensional ESPRIT. The CP method has been reported to have lower computational complexity than SSD but pairing accuracy equivalent to SSD. However, the CP method is known to ouput incorrect pairs when multiple identical parameters occur in any of the domains. Therefore, in this paper, we introduce a new algorithm called the improved CP method, which is presented in the following section.

2) PROPOSED MULTIDIMENSIONAL CP METHOD

In this section, we propose an accurate multidimensional CP method called the improved CP method. Specifically, a 4D pairing procedure is provided below. First, the eigenvalue decomposition of Eq. (24) is performed four times for the domain pairs $(i, j) = (1, 2), (2, 3), (3, 4), (4, 1)$ to calculate $(\omega_1^{(12)}(l), \omega_2^{(12)}(l))$, $(\omega_2^{(23)}(l), \omega_3^{(23)}(l))$, $(\omega_3^{(34)}(l), \omega_4^{(34)}(l))$, and $(\omega_4^{(41)}(l), \omega_1^{(41)}(l))$ for $l = 1, 2, \cdots, L$. Note that these parameters are paired between two domains only in each case, which means that they are not yet associated over all four domains.

To associate these parameters over all four domains, it is necessary to determine the most likely index combinations $l_{12}, l_{23}, l_{34}, l_{41}$, where $l = l_{12}$ represents a paired index between domains 1 and 2, and l is used as an independent variable hereafter. Because the parameters are already associated for the adjacent domain pairs (1, 2), (2, 3), (3, 4), and (4, 1), the number of degrees of freedom is three. To optimize the indices l_{23}, l_{34}, and l_{41} for $l = l_{12}$, the evaluation function $\Delta_l(l_{23}, l_{34}, l_{41})$ is introduced as follows:

$$\begin{aligned}\Delta_l(l_{23}, l_{34}, l_{41}) = &\left\{\omega_1{}^{(41)}(l_{41}) - \omega_1{}^{(12)}(l)\right\}^2 \\ &+ \left\{\omega_2{}^{(12)}(l) - \omega_2{}^{(23)}(l_{23})\right\}^2 \\ &+ \left\{\omega_3{}^{(23)}(l_{23}) - \omega_3{}^{(34)}(l_{34})\right\}^2 \\ &+ \left\{\omega_4{}^{(34)}(l_{34}) - \omega_4{}^{(41)}(l_{41})\right\}^2. \quad (27)\end{aligned}$$

The sum of the evaluation functions $\sum_{l=1}^{L} \Delta_l(l_{23}^{(l)}, l_{34}^{(l)}, l_{41}^{(l)})$ is minimized via a brute force optimization procedure by checking all possible combinations. In each domain, the same index cannot be selected more than once to prevent incorrect association. The possible combinations are given as permutations of the L indices and the number of permutations in each domain is $L!$, which results in a total of $(L!)^3$ combinations for three domains while excluding the ordered index $l = l_{12}$. Note that each of the unknown variables of the evaluation function have a superscript (l) because these indices depend on index l. As a result, the optimum indices $(l, \hat{l}_{23}^{(l)}, \hat{l}_{34}^{(l)}, \hat{l}_{41}^{(l)})$ are obtained as $(1, \hat{l}_{23}^{(1)}, \hat{l}_{34}^{(1)}, \hat{l}_{41}^{(1)}), (2, \hat{l}_{23}^{(2)}, \hat{l}_{34}^{(2)}, \hat{l}_{41}^{(2)}), \cdots, (L, \hat{l}_{23}^{(L)}, \hat{l}_{34}^{(L)}, \hat{l}_{41}^{(L)})$.

Finally, the parameters $\hat{\mu}_i(l)$ $(l = 1, 2, \cdots, L)$ that are paired over the four domains are obtained using the averaged eigenvalues as follows:

$$\hat{\mu}_1(l) = 2\tan^{-1}\left[\left(\omega_1^{(41)}(\hat{l}_{41}^{(l)}) + \omega_1^{(12)}(l)\right)/2\right], \quad (28)$$

$$\hat{\mu}_2(l) = 2\tan^{-1}\left[\left(\omega_2^{(12)}(l) + \omega_2^{(23)}(\hat{l}_{23}^{(l)})\right)/2\right], \quad (29)$$

$$\hat{\mu}_3(l) = 2\tan^{-1}\left[\left(\omega_3^{(23)}(\hat{l}_{23}^{(l)}) + \omega_3^{(34)}(\hat{l}_{34}^{(l)})\right)/2\right], \quad (30)$$

$$\hat{\mu}_4(l) = 2\tan^{-1}\left[\left(\omega_3^{(34)}(\hat{l}_{34}^{(l)}) + \omega_3^{(41)}(\hat{l}_{41}^{(l)})\right)/2\right]. \quad (31)$$

Because the improved CP method calculates $\sum_{l=1}^{L} \Delta_l(l_{12}^{(l)}, l_{23}^{(l)}, l_{34}^{(l)})$ for all $(L!)^3$ possible combinations, the computational complexity of this method becomes greater as L increases. However, our signal separation technique using multidimensional ESPRIT is only required when multiple targets are located at almost the same distance from the antenna array. Because the proposed method is designed for a UWB radar system with high-range resolution, it is unlikely to have more than three targets within the same range bin, which means that L is typically two or three at most. Therefore, the computational complexity of the improved CP method is not a problem in practice.

Algorithm 1 Estimation of Target Position $\hat{\boldsymbol{y}}_l$

1: Compute the correlation matrix $\boldsymbol{R}_{xx}$.
2: Compute the eigenvalues λ_i and eigenvectors $\boldsymbol{v}_i$ of $\boldsymbol{R}_{xx}$ $(i = 1, \cdots, M_{\mathrm{sub}})$.
3: Estimate the number of targets L using MDL(l).
4: Compute Υ_i for $i = 1, 2, 3, 4$ using $E_{\mathrm{s}} = [\boldsymbol{v}_1 \cdots \boldsymbol{v}_L]$ and Eq. (19).
5: Compute $\omega_1^{(12)}(l), \omega_2^{(12)}(l), \cdots, \omega_1^{(31)}(l)$ using Eqs. (24)–(26).
6: Estimate $\hat{\mu}_i(l)$ using Eqs. (28)–(31).
7: Estimate the target positions $\hat{\boldsymbol{y}}_l$ using Eq. (32).

D. ESTIMATION OF THE TARGET POSITION

In the previous section, we explained how to estimate the 4D paired estimation parameters $\hat{\mu}_i(l)$. Using Eq. (2) and parameters $\hat{\mu}_i(l)$, we can estimate velocity $\hat{v}_l$, range $\hat{r}_l$, and DOAs $\hat{\theta}_{l1}$ and $\hat{\theta}_{l2}$. The 3D position of the l-th target $\hat{\boldsymbol{y}}_l$ is finally obtained as follows:

$$\hat{\boldsymbol{y}}_l = \begin{bmatrix} \hat{r}_l \sin\hat{\theta}_{l1} \\ \hat{r}_l\sqrt{\cos^2\hat{\theta}_{l1} - \sin^2\hat{\theta}_{l2}} \\ \hat{r}_l \sin\hat{\theta}_{l2} \end{bmatrix}. \quad (32)$$

Algorithm 1 summarizes the algorithm that estimates the 3D positions of L targets. This algorithm is executed every $\Delta t_{\mathrm{r}} (= M_3 \Delta t)$ and we then obtain the target parameters $\hat{v}_l(n\Delta t_{\mathrm{r}})$, $\hat{\theta}_{l1}(n\Delta t_{\mathrm{r}})$, $\hat{\theta}_{l2}(n\Delta t_{\mathrm{r}})$, $\hat{r}_l(n\Delta t_{\mathrm{r}})$, and $\hat{\boldsymbol{y}}_l(n\Delta t_{\mathrm{r}})$ for $n = 1, 2, 3, \cdots$. The accuracy of these estimates is discussed in the following section.

IV. SIMULATION AND PERFORMANCE EVALUATION

A. SIMULATION SETTINGS AND PARAMETERS

We evaluated the multidimensional ESPRIT-based imaging method using simulations. In these simulations, we assumed the presence of a single transmitting element at the origin and a square-shaped planer array with $M_1 \times M_2$ elements, where $M_1 = M_2 = 3$. The transmitted signal was a UWB signal with center frequency $f_{\mathrm{c}} = 79.0$ GHz, center wavelength $\lambda_{\mathrm{c}} = 3.8$ mm, and -3 dB bandwidth $W = 800$ MHz. The signal waveform is Gaussian as $s(t) = \exp(-t^2/2\sigma_{\mathrm{c}}^2)$, where σ_{c} is $\sigma_{\mathrm{c}} = \sqrt{\ln 2}/\pi W = 0.33$ ns. Slow-time sampling interval $\Delta T = 0.24$ ms, fast-time sampling interval $\Delta\tau = 0.5$ ns, range sampling interval $\Delta r = 75$ mm, and element spacing $\Delta d = 2.26$ mm $(0.6\lambda_{\mathrm{c}})$ in the receiving array.

Nine-channel signals were recorded over a period of $t_{\max} = 0.95$ s, which corresponded to the number of time samples $N_{\mathrm{s}} = t_{\max}/\Delta T = 4 \times 10^3$. The target positions $\boldsymbol{y}_1(t)$, $\boldsymbol{y}_2(t)$ and $\boldsymbol{y}_3(t)$ $(0 \le t \le t_{\max})$ were uniform and spiral motions as follows:

$$\boldsymbol{y}_1(t) = \begin{bmatrix} 0 \\ r_0 + v_0 t \\ 0 \end{bmatrix},$$

$$\boldsymbol{y}_2(t) = \begin{bmatrix} r_{\mathrm{rad}} \cos(t/t_{\max} - \pi/3) \\ r_0 + v_0\, t \\ r_{\mathrm{rad}} \sin(t/t_{\max} - \pi/3) \end{bmatrix},$$

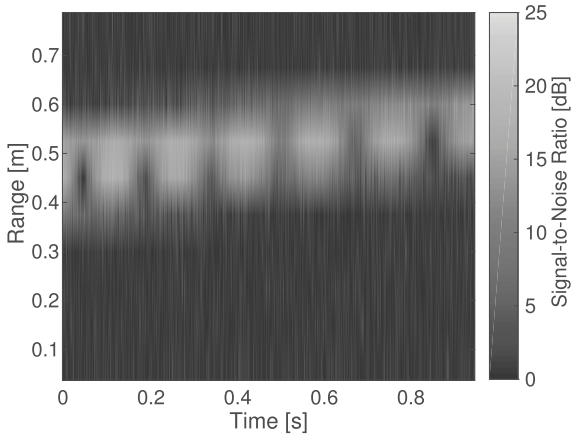

FIGURE 2. Received signal power of $\mathrm{Rx}_{2,2}$ as a function of slow time and range.

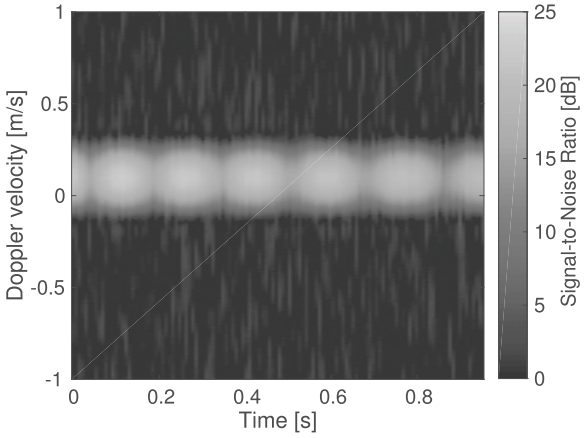

FIGURE 3. Received signal power of $\mathrm{Rx}_{2,2}$ as a function of slow time and Doppler velocity.

$$\boldsymbol{y}_3(t) = \begin{bmatrix} r_{\mathrm{rad}} \cos\left(t/t_{\max} - 5\pi/6\right) \\ r_0 + v_0\, t \\ r_{\mathrm{rad}} \sin\left(t/t_{\max} - 5\pi/6\right) \end{bmatrix}, \tag{33}$$

where $r_0 = 0.425$ m, $r_{\mathrm{rad}} = 0.250$ m and $v_0 = 0.100$ m/s. Note that the target positions and motions were selected to simulate one of the worst case scenarios, in which multiple targets could not be separated within any of the range, Doppler, or DOA domains. The received signals were simulated numerically using a ray tracing procedure, in which, we did not consider occurrences of multiple scattering. The SNR was set to SNR $= 20$ dB, where the SNR is defined as the ratio of the peak signal power to the noise power in the time domain after the application of the filter.

Fig. 2 shows the SNR of the signal received by $\mathrm{Rx}_{2,2}$ as a function of a slow time and range. Fig. 3 shows the SNR of the same received signal as a function of a slow time and Doppler velocity, where the spectrogram was obtained using the short-time Fourier transform (STFT) with a Hann window of size 15.4 ms ($= 64\Delta T$). In these figures, the echo signals from the three targets could not be separated either within the range or frequency domains because the range differences between the targets were between 57.0 mm and 68.1 mm, and their differences in Doppler velocity were also larger than the frequency resolution. Hence, these echoes could not be separated, even when using high-resolution UWB radar, without the aid of an adaptive signal processing technique such as ESPRIT.

The number of slow-time samples used for the 4D ESPRIT was $M_3 = 64$. The frequency band used for the 4D ESPRIT was $f_{\mathrm{c}} - W_{\mathrm{e}}/2 \leq f \leq f_{\mathrm{c}} + W_{\mathrm{e}}/2$, where $W_{\mathrm{e}} = 800$ MHz, which is the same as the -3 dB bandwidth W, and the frequency domain interval was $\Delta f = 200$ MHz. Under these conditions, $M_4 = \lfloor W_{\mathrm{e}}/\Delta f \rfloor + 1 = 5$. Four-dimensional smoothing was then performed with $M_{\mathrm{sub1}} = 2$, $M_{\mathrm{sub2}} = 2$, $M_{\mathrm{sub3}} = 32$, and $M_{\mathrm{sub4}} = 3$. We set the estimation time interval to $t_{\mathrm{r}} = M_{\mathrm{sub3}}\Delta T = 7.62$ ms.

In the above assumption, the theoretical maximum number of targets $L'_{\max}$ that can be separated using 4D unitary ESPRIT is $L'_{\max} = M_{\mathrm{sub}} = 384$. However, the actual maximum number of targets $L_{\max}(\leq L'_{\max})$ that can be separated depends on the locations and motions of the targets, in addition to the resolution in each dimension, which is limited by multiple factors, such as the echo S/N ratio, correlation coefficient between echoes, and chain pairing accuracy.

B. COMPARISON WITH OTHER ESPRIT-BASED METHODS

In this section, we introduce two other conventional ESPRIT-based methods (denoted by method 1 and method 2) for comparison. Method 1 was proposed by the authors [21], and applies a STFT to obtain the time-frequency distribution of the received signal. If echoes with different Doppler velocities are separated in the frequency domain, then the two DOAs of each echo can be estimated using the 2-D unitary ESPRIT method in the spatial domain, where the 2D unitary ESPRIT method is applied to each of the significant peaks of the time-frequency distribution. If echoes with similar Doppler velocities cannot be separated in the frequency domain, then method 1 produces incorrect imaging results.

Method 2, however, applies the 3D unitary ESPRIT method in the frequency domain and two spatial domains for joint estimation of the Doppler velocity and two DOAs [25]. These two methods both use the range interpolation method, which is also known as the P1/P2 method, to estimate the range of each target [21]. In methods 1 and 2, the numbers of slow-time samples and numbers of smoothing data samples for the unitary ESPRIT method were both set to the same values as those of the 4D ESPRIT for fair comparison. Additionally, the actual number of targets was assumed to be known for methods 1 and 2, whereas the number of targets was assumed to be unknown for the 4D ESPRIT-based method; this gives a handicap to the 4D method to allow us to evaluate the upper performance limits of methods 1 and 2.

C. DEFINITIONS OF ACCURACY

To evaluate the performance of these methods, the root-mean-square error (RMSE) was used to assess accuracy in terms of

the target position $\hat{\boldsymbol{y}}_l(k\Delta t_{\rm r})$, Doppler velocity $\hat{v}_l(k\Delta t_{\rm r})$, target range $\hat{r}_l(k\Delta t_{\rm r})$, and target DOAs $\hat{\theta}_{l1}(k\Delta t_{\rm r})$ and $\hat{\theta}_{l2}(k\Delta t_{\rm r})$.

For example, the RMSE of $\hat{\boldsymbol{y}}_l(k\Delta t_{\rm r})$ was evaluated as follows:

$$\mathrm{RMSE}_y = \sqrt{\frac{1}{K}\sum_{k=1}^{K}\frac{1}{\hat{L}(k\Delta t_{\rm r})}\sum_{l=1}^{\hat{L}(k\Delta t_{\rm r})}\mathrm{err}_l^{(y)}(k\Delta t_{\rm r})}, \quad (34)$$

$$\mathrm{err}_l^{(y)}(k\Delta t_{\rm r}) = \min_j \|\hat{\boldsymbol{y}}_l(k\Delta t_{\rm r}) - \boldsymbol{y}_j(k\Delta t_{\rm r})\|^2, \quad (35)$$

where $\boldsymbol{y}_j(k\Delta t_{\rm r})$ denotes the actual position of the j-th target at time $t = k\Delta t_{\rm r}$, K is the number of updates using the ESPRIT-based methods, and $\hat{L}(k\Delta t_{\rm r})$ is the estimated number of targets at time $t = k\Delta t_{\rm r}$. In the two conventional methods, the number of targets $\hat{L}(k\Delta t_{\rm r})$ was always set to three because the number of targets was assumed to be known for these methods. In the 4D method, however, the number of targets was estimated using the MDL-based method that was presented in Section III-B.

The RMSEs in $\hat{v}_l(k\Delta t_{\rm r})$, $\hat{r}_l(k\Delta t_{\rm r})$, $\hat{\theta}_{l1}(k\Delta t_{\rm r})$, and $\hat{\theta}_{l2}(k\Delta t_{\rm r})$ were also evaluated using Eq. (34), but with different definitions of the errors: $\mathrm{err}_l^{(v)}(k\Delta t_{\rm r})$, $\mathrm{err}_l^{(r)}(k\Delta t_{\rm r})$, $\mathrm{err}_l^{(\theta_1)}(k\Delta t_{\rm r})$, and $\mathrm{err}_l^{(\theta_2)}(k\Delta t_{\rm r})$, rather than $\mathrm{err}_l^{(y)}(k\Delta t_{\rm r})$:

$$\mathrm{err}_l^{(v)}(k\Delta t_{\rm r}) = \min_j \left\{\hat{v}_l(k\Delta t_{\rm r}) - v_j(k\Delta t_{\rm r})\right\}^2, \quad (36)$$

$$\mathrm{err}_l^{(r)}(k\Delta t_{\rm r}) = \min_j \left\{\hat{r}_l(k\Delta t_{\rm r}) - r_j(k\Delta t_{\rm r})\right\}^2, \quad (37)$$

$$\mathrm{err}_l^{(\theta_1)}(k\Delta t_{\rm r}) = \min_j \left\{\hat{\theta}_{l1}(k\Delta t_{\rm r}) - \theta_{j1}(k\Delta t_{\rm r})\right\}^2, \quad (38)$$

$$\mathrm{err}_l^{(\theta_2)}(k\Delta t_{\rm r}) = \min_j \left\{\hat{\theta}_{l2}(k\Delta t_{\rm r}) - \theta_{j2}(k\Delta t_{\rm r})\right\}^2, \quad (39)$$

where $v_j(k\Delta t_{\rm r})$, $r_j(k\Delta t_{\rm r})$, $\theta_{j1}(k\Delta t_{\rm r})$, and $\theta_{j2}(k\Delta t_{\rm r})$ denote the actual Doppler velocity, range, and DOAs, respectively, of the j-th target at time $t = k\Delta t_{\rm r}$.

D. PERFORMANCE EVALUATION OF THE THREE IMAGING METHODS

Figs. 4-6 show the imaging results for conventional method 1, conventional method 2, and the 4D method, respectively. In these figures, black lines indicate the actual target position trajectories, whereas circles indicate the estimated positions $\hat{\boldsymbol{y}}_l(k\Delta t_{\rm r})$ for each time step. As shown in Fig. 4, the target positions that were estimated using method 1 deviated from the actual trajectories because the gap between the target velocities was too small to allow the targets to be separated in the frequency domain. Simultaneously, Figs. 5 and 6 show that method 2 and the 4D method both estimated the target trajectories more accurately than method 1, although incorrect estimates were also found in these images. The RMSEs for the three methods are provided in Table 1.

Figs. 7–9 show the Doppler velocities that were estimated using conventional methods 1 and 2, and the 4D method, respectively. Targets 2 and 3 with their spiral motions always had almost the same Doppler velocity, whereas target 1 with its uniform motion had a lower Doppler velocity. Therefore, in each figure, we see two lines that show the actual Doppler velocities. Because method 1 attempted to separate the echoes in the frequency domain using the

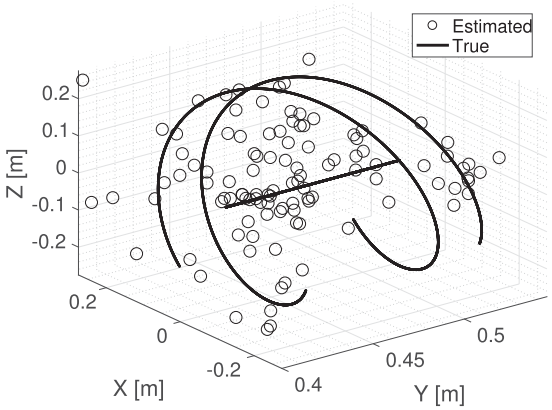

FIGURE 4. Imaging results obtained using conventional method 1.

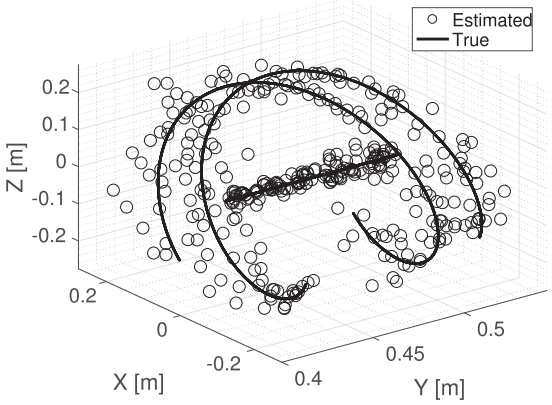

FIGURE 5. Imaging results obtained using conventional method 2.

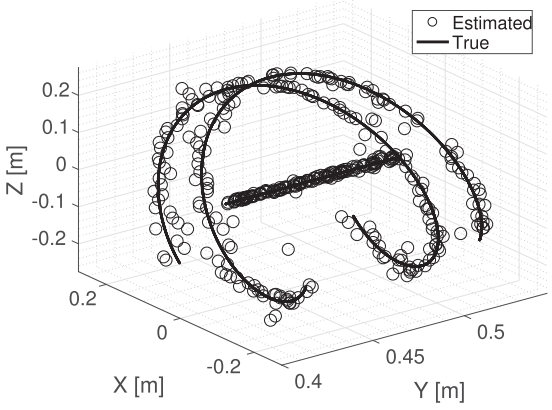

FIGURE 6. Imaging results obtained using the 4D method.

TABLE 1. RMSEs of $\hat{v}_l(k\Delta t_{\rm r})$, $\hat{\theta}_{l1}(k\Delta t_{\rm r})$, $\hat{\theta}_{l2}(k\Delta t_{\rm r})$, $\hat{r}_l(k\Delta t_{\rm r})$, and $\hat{y}_l(k\Delta t_{\rm r})$ for each imaging method.

Method	$\hat{v}_l$ (mm/s)	$\hat{\theta}_{l1}$ (rad)	$\hat{\theta}_{l2}$ (rad)	$\hat{r}_l$ (mm)	$\hat{\boldsymbol{y}}_l$ (mm)
Method 1	4.8	0.461	0.447	33.7	409.1
Method 2	34.0	0.048	0.070	3.3	49.2
4-D method	1.3	0.022	0.039	1.9	26.3

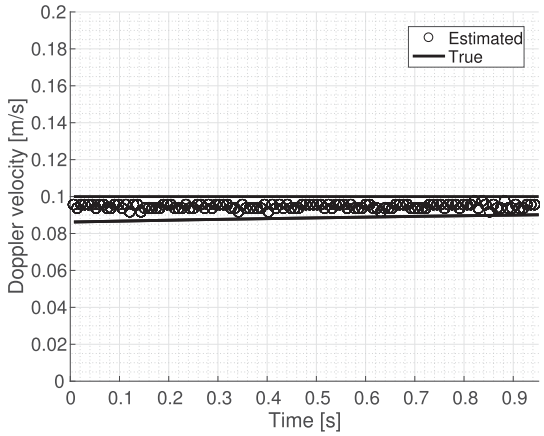

FIGURE 7. Doppler velocity estimation results obtained using conventional method 1.

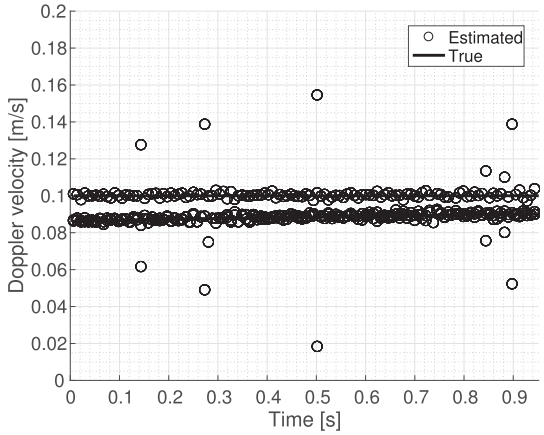

FIGURE 8. Doppler velocity estimation results obtained using conventional method 2.

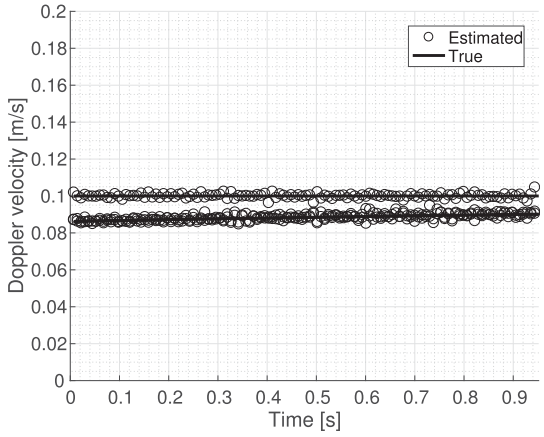

FIGURE 9. Doppler velocity estimation results obtained using the 4D method.

traditional Fourier transform-based spectrum, these echoes could not be distinguished because of the limitations of the frequency resolution of the Fourier transform (Fig. 7). In contrast, as shown in Fig. 8, method 2 separated the two Doppler velocities using the 3D unitary ESPRIT method. Surprisingly, however, the accuracy of method 2 was worse than that of method 1 in terms of the Doppler velocity,

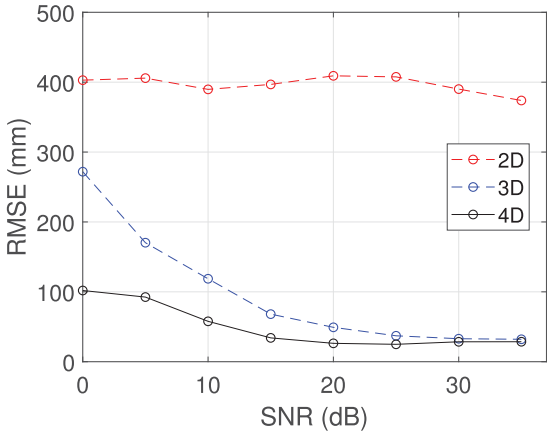

FIGURE 10. RMSEs in $\hat{\boldsymbol{y}}_l$ versus SNR.

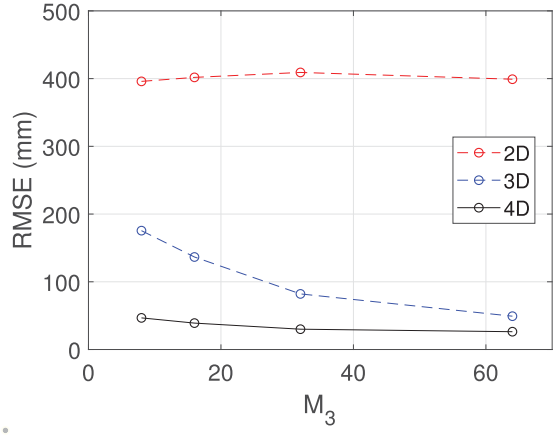

FIGURE 11. RMSEs in $\hat{\boldsymbol{y}}_l$ versus M_3.

as shown in Table 1. This is because the Doppler velocity that was estimated using method 2 had extremely large errors that lay outside the range of Fig. 8; these errors were caused by the interference of multiple echoes. By contrast, the accuracy of the 4D method for estimating the Doppler velocity was higher than that of both methods 1 and 2, and the two Doppler velocity curves were estimated accurately, as shown in Fig. 9.

Table 1 shows the remarkable improvement in accuracy of the estimation of all parameters when using the 4D method. The accuracy of the 4D method was 15.6 times higher than that of method 1 and 1.87 times higher than that of method 2. These results indicate that the higher-dimensional ESPRIT method separated multiple radar echoes more accurately than methods 1 and 2, thus achieving higher space-time-frequency resolution. This occurred because even if the echoes cannot be separated in one specific domain, they may still be able to be separated in the other domains. Therefore, the process of joint estimation of multiple parameters (i.e., the range, Doppler frequency and DOAs) is promising for the realization of high-resolution radar imaging.

The RMSEs in estimating $\hat{\boldsymbol{y}}_l$ versus SNR are shown in Fig. 10. The figure shows that 4D unitary ESPRIT achieved high accuracy even for a relatively low SNR. Fig. 11 shows the RMSEs in $\hat{\boldsymbol{y}}_l$ versus the number of time

samples M_3, where SNR was set to 20 dB. This figure shows that regardless of M_3, 4D unitary ESPRIT achieved the highest accuracy among the three methods. The RMSEs in estimating various parameters using a high-dimensional ESPRIT algorithm and similar techniques were reported in studies [25], [27], [30], [31].

E. COMPUTATIONAL COMPLEXITY

As stated in the Introduction, multidimensional adaptive signal processing is considered to be impractical in many applications because of its computational complexity, particularly that of multidimensional peak searches. This was the motivation for introducing the multidimensional unitary ESPRIT method used in this study. In this section, we discuss the computational complexity of the 4D method and compare it with the complexities of conventional methods 1 and 2 that were discussed in the previous section.

All three methods require eigenvalue decomposition of the correlation matrix R_{xx} in the unitary ESPRIT method. The number of operations required for eigenvalue decomposition of an $n \times n$ matrix is denoted by $O(n^3)$ [36]. For method 1, the matrix size of R_{xx} is $M_{\mathrm{sub}1}M_{\mathrm{sub}2} \times M_{\mathrm{sub}1}M_{\mathrm{sub}2}$, and thus $n^3 = (M_{\mathrm{sub}1}M_{\mathrm{sub}2})^3 = 64$. Similarly, for method 2, $n^3 = (M_{\mathrm{sub}1}M_{\mathrm{sub}2}M_{\mathrm{sub}3})^3 = 2.1 \times 10^6$, whereas for the 4D method, $n^3 = (M_{\mathrm{sub}1}M_{\mathrm{sub}2}M_{\mathrm{sub}3}M_{\mathrm{sub}4})^3 = 5.7 \times 10^7$. The number of operations required increases because of the multidimensionalization involved in the multidimensional ESPRIT algorithms. However, because of the system costs involved, the number of antenna elements cannot be high. Additionally, in real-time applications such as human monitoring in healthcare, the number of slow-time samples must be limited to prevent response delays. Consideration of these factors allows the computational complexity of the 4D method to be maintained within a practical range.

With respect to the number of multiplications, the computational complexities of the Wiener filter and minimum description length are $O(M)$ and $O(L_{\max}M_{\mathrm{sub}}^2)$, respectively. As long as $L_{\max}$ and M_{sub} are assumed to be small, the calculation time for these steps remains small. The computational complexity for the multidimensional CP method was discussed in Section III-C. Fig. 12 shows the average running time of the three algorithms versus the number of time samples M_3, where the algorithms were executed in MATLAB running on a laptop computer: ASUS ZenBook S UX391UA with an Intel(R) Core(TM) i7-8550U 1.80-GHz processor and 16 GB of RAM. Note that the algorithms could run faster if implemented in a compiled language instead of a scripting language such as MATLAB. The computational time of the high-dimensional ESPRIT algorithm and similar techniques can be found in previous studies [30], [31].

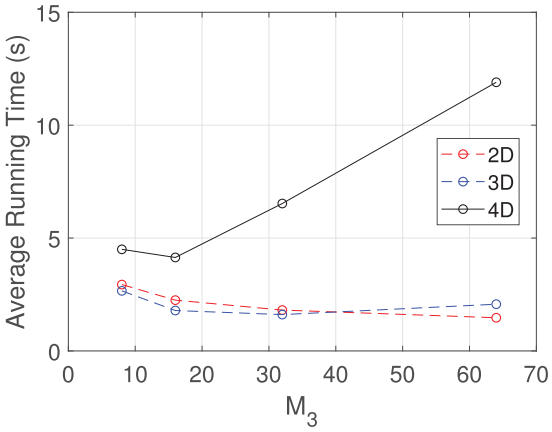

FIGURE 12. Average running time versus M_3.

V. DISCUSSION

A. SIGNIFICANCE OF SUPER-RESOLUTION IN UWB RADAR IMAGING

The main contributions of this study are as follows: (1) 4D unitary ESPRIT was applied for the first time to the near-field UWB radar imaging of multiple moving targets; and (2) the near-field imaging accuracy of 4D unitary ESPRIT was compared with those of the 2D and 3D unitary ESPRIT algorithms.

Because a human body can be modeled as a collection of multiple scattering centers moving in close proximity, this study's target model can be associated with practical human monitoring applications, including human activity classification and human position tracking. Echoes from human body parts cannot be separated unless a sufficiently high resolution is achieved. In this respect, super resolution techniques (e.g., ESPRIT) are necessary to maximize the functionality of UWB radar systems in such applications. The results of this study suggest the potential efficacy of the 4D unitary ESPRIT algorithm in improving the accuracy and resolution of radar measurement in such applications.

Radar-based human monitoring (e.g., human activity classification and differentiating multiple people in a room) is an increasingly popular application of UWB radar systems, whose performance can be largely improved using 4D unitary ESPRIT. Regarding the example of classifying human activity, the classification accuracy is expected to be improved by using 4D unitary ESPRIT to improve the velocity resolution, which would generate a detailed time–frequency distribution (spectrogram) and allow the accurate classification of human activity. Regarding the other example of differentiating two people, performance is also expected to be improved by enhancing the spatial and velocity resolutions using 4D unitary ESPRIT to separate echoes in the spatial and frequency domains and also to distinguish the micro-Doppler patterns of the people. The application of the 4D unitary ESPRIT algorithm to these human monitoring applications is an important research topic for future studies.

B. NEAR- AND FAR-FIELD RADAR AND SUPER-RESOLUTION

The use of 4D unitary ESPRIT can improve the resolution of both near- and far-field radar measurements. However,

high-resolution techniques in the frequency domain generally require both a high S/N ratio and wide bandwidth, which are difficult to achieve in far-field measurement. Far-field radar measurement requires a relatively narrow bandwidth to ensure a sufficient S/N ratio, which limits the use of high-resolution techniques. Additionally, for far-field radar measurement applications, the detectability of targets is often more important than the resolution. By contrast, for targets in the near field, the echo S/N ratio is relatively high, even with a wide bandwidth (e.g., UWB), which allows for the use of high-resolution techniques for the accurate measurement of multiple moving targets. Therefore, the introduction of UWB near-field radar makes it possible to achieve super-resolution imaging. Additionally, as mentioned above, near-field radar measurement has potential applications, such as the measurement of moving human body parts, whereas far-field radar measurement rarely considers multiple targets moving independently in close proximity. This discussion suggests that 4D unitary ESPRIT can play a more important role when applied to near-field radar measurement.

VI. CONCLUSION

In this paper, we applied the 4D unitary ESPRIT algorithm to UWB radar imaging of near-field distributed targets, which enabled the joint estimation of the Doppler velocity, range, and DOAs of targets using MDL-based target number estimation and an improved CP method. We evaluated and compared the imaging accuracies of the 4D, 3D, and 2D algorithms. The two low-dimensional algorithms were based on the 2D and 3D unitary ESPRIT methods. Using numerical simulations with three targets moving in close proximity, we demonstrated that the 4D method improved imaging accuracy by 15.6 and 1.87 times when compared with the two low-dimensional algorithms. These simulation results indicate the remarkable potential of the multi-dimensional ESPRIT algorithm to achieve high-resolution radar imaging with UWB radar while maintaining the computational complexity within a practical range. The next step of this study will be actual radar measurement using UWB array antennas to experimentally verify the performance of near-field imaging using the 4D unitary ESPRIT algorithm.

APPENDIX

4D SMOOTHING

Correlation matrix R_{xx} after N_1, N_2, N_3, and N_4 smoothing operations in each dimension and the total number of smoothing operations $N = N_1\, N_2\, N_3\, N_4$ is expressed as follows:

$$R_{xx} = \frac{1}{N}\mathrm{Re}\left\{ Q_{M_{\mathrm{sub}}}^{\mathrm{H}} \sum_{n_1=1}^{N_1}\sum_{n_2=1}^{N_2}\sum_{n_3=1}^{N_3}\sum_{n_4=1}^{N_4} R^{(*)} Q_{M_{\mathrm{sub}}} \right\}, \quad (40)$$

$$R^{(*)} = \boldsymbol{x}_{n_1,n_2,n_3,n_4}\boldsymbol{x}_{n_1,n_2,n_3,n_4}^{\mathrm{H}}, \quad (41)$$

$$\boldsymbol{x}_{n_1,n_2,n_3,n_4} = \begin{bmatrix} x_{n_1,n_2,n_3,n_4} \\ x_{n_1+1,n_2,n_3,n_4} \\ \vdots \\ x_{n_1+M_{\mathrm{sub}1}-1,n_2,n_3,n_4} \\ x_{n_1,n_2+1,n_3,n_4} \\ \vdots \\ x_{n_1+M_{\mathrm{sub}1}-1,n_2+M_{\mathrm{sub}2}-1,n_3,n_4} \\ x_{n_1,n_2,n_3+1,n_4} \\ \vdots \\ x_{n_1+M_{\mathrm{sub}1}-1,n_2+M_{\mathrm{sub}2}-1,n_3+M_{\mathrm{sub}3}-1,n_4} \\ x_{n_1,n_2,n_3,n_4+1} \\ \vdots \\ x_{n_1+M_{\mathrm{sub}1}-1,n_2+M_{\mathrm{sub}2}-1,n_3+M_{\mathrm{sub}3}-1,n_4+M_{\mathrm{sub}4}-1} \end{bmatrix}, \quad (42)$$

where $M_{\mathrm{sub}i}$ is expressed as $M_{\mathrm{sub}i} = M_i - N_i + 1$ for $i = 1, 2, 3, 4$. The orders of M_1, M_2, M_3, and M_4 decrease from M_i to $M_{\mathrm{sub}i}$ for $i = 1, 2, 3, 4$ through the smoothing process, and the total degree also decreases from M to $M_{\mathrm{sub}} = M_{\mathrm{sub}1}M_{\mathrm{sub}2}M_{\mathrm{sub}3}M_{\mathrm{sub}4}$. Use of the smoothing process is expected to suppress the correlation between signals among the L echoes.

REFERENCES

[1] Y. Kim and H. Ling, "Human activity classification based on micro-Doppler signatures using a support vector machine," *IEEE Trans. Geosci. Remote Sens.*, vol. 47, no. 5, pp. 1328–1337, May 2009.

[2] J. D. Bryan, J. Kwon, N. Lee, and Y. Kim, "Application of ultra-wide band radar for classification of human activities," *IET Radar, Sonar Navigat.*, vol. 6, no. 3, pp. 172–179, Mar. 2012.

[3] J. A. Nanzer, "A review of microwave wireless techniques for human presence detection and classification," *IEEE Trans. Microw. Theory Techn.*, vol. 65, no. 5, pp. 1780–1794, May 2017.

[4] F. Qi, F. Liang, M. Liu, H. Lv, P. Wang, H. Xue, and J. Wang, "Position-information-indexed classifier for improved through-wall detection and classification of human activities using UWB bio-radar," *IEEE Antennas Wireless Propag. Lett.*, vol. 18, no. 3, pp. 437–441, Mar. 2019.

[5] Y. Lin, J. Le Kernec, S. Yang, F. Fioranelli, O. Romain, and Z. Zhao, "Human activity classification with radar: Optimization and noise robustness with iterative convolutional neural networks followed with random forests," *IEEE Sensors J.*, vol. 18, no. 23, pp. 9669–9681, Dec. 2018.

[6] B. Y. Su, K. C. Ho, M. J. Rantz, and M. Skubic, "Doppler radar fall activity detection using the wavelet transform," *IEEE Trans. Biomed. Eng.*, vol. 62, no. 3, pp. 865–875, Mar. 2015.

[7] R. J. Javier and Y. Kim, "Application of linear predictive coding for human activity classification based on micro-Doppler signatures," *IEEE Geosci. Remote Sens. Lett.*, vol. 11, no. 10, pp. 1831–1834, Oct. 2014.

[8] B. Çağliyan and S. Z. Gürbüz, "Micro-Doppler-based human activity classification using the mote-scale BumbleBee radar," *IEEE Geosci. Remote Sens. Lett.*, vol. 12, no. 10, pp. 2135–2139, Oct. 2015.

[9] J. A. Nanzer and R. L. Rogers, "Bayesian classification of humans and vehicles using micro-Doppler signals from a scanning-beam radar," *IEEE Microw. Wireless Compon. Lett.*, vol. 19, no. 5, pp. 338–340, May 2009.

[10] A. Ghaleb, L. Vignaud, and J. M. Nicolas, "Micro-Doppler analysis of wheels and pedestrians in ISAR imaging," *IET Signal Process.*, vol. 2, no. 3, pp. 301–311, Sep. 2008.

[11] Z. Peng, J. M. Muñoz-Ferreras, Y. Tang, C. Liu, R. Gómez-García, L. Ran, and C. Li, "A portable FMCW interferometry radar with programmable low-IF architecture for localization, ISAR imaging, and vital sign tracking," *IEEE Trans. Microw. Theory Techn.*, vol. 65, no. 4, pp. 1334–1344, Apr. 2017.

[12] Y. Li, Z. Peng, R. Pal, and C. Li, "Potential active shooter detection based on radar micro-Doppler and range-Doppler analysis using artificial neural network," *IEEE Sensors J.*, vol. 19, no. 3, pp. 1052–1063, Feb. 2019.
[13] Y. He, P. Molchanov, T. Sakamoto, P. Aubry, F. L. Chevalier, and A. Yarovoy, "Range-Doppler surface: A tool to analyse human target in ultra-wideband radar," *IET Radar, Sonar Navigat.*, vol. 9, no. 9, pp. 1240–1250, Dec. 2015.
[14] A. Lin and H. Ling, "Frontal imaging of human using three-element Doppler and direction-of-arrival radar," *Electron. Lett.*, vol. 42, no. 11, pp. 660–661, May 2006.
[15] A. Lin and H. Ling, "Doppler and direction-of-arrival (DDOA) radar for multiple-mover sensing," *IEEE Trans. Aerosp. Electron. Syst.*, vol. 43, no. 4, pp. 1496–1509, Oct. 2007.
[16] K. Saho, T. Sakamoto, T. Sato, K. Inoue, and T. Fukuda, "Pedestrian imaging using UWB Doppler radar interferometry," *IEICE Trans. Commun.*, vol. E96-B, pp. 613–623, Feb. 2013.
[17] K. Saho, H. Homma, T. Sakamoto, T. Sato, K. Inoue, and T. Fukuda, "Accurate image separation method for two closely spaced pedestrians using UWB Doppler imaging radar and supervised learning," *IEICE Trans. Commun.*, vol. E97-B, pp. 1223–1233, Jun. 2014.
[18] S. S. Ram and H. Ling, "Through-wall tracking of human movers using joint Doppler and array processing," *IEEE Geosci. Remote Sens. Lett.*, vol. 5, no. 3, pp. 537–541, Jul. 2008.
[19] S. S. Ram and A. Majumdar, "High-resolution radar imaging of moving humans using Doppler processing and compressed sensing," *IEEE Trans. Aerosp. Electron. Syst.*, vol. 51, no. 2, pp. 1279–1287, Apr. 2015.
[20] M. Anabuki, S. Okumura, T. Sakamoto, K. Saho, T. Sato, M. Yoshioka, K. Inoue, T. Fukuda, and H. Sakai, "Ultrawideband radar imaging using adaptive array and Doppler separation," *IEEE Trans. Aerosp. Electron. Syst.*, vol. 53, no. 1, pp. 190–200, Feb. 2017.
[21] M. Anabuki, S. Okumura, T. Sakamoto, K. Saho, T. Sato, M. Yoshioka, K. Inoue, T. Fukuda, and H. Sakai, "High-resolution imaging and separation of multiple pedestrians using UWB Doppler radar interferometry with adaptive beamforming technique," in *Proc. 11th Eur. Conf. Antennas Propag.*, Paris, France, Mar. 2017, pp. 469–473.
[22] J. Ward, "Maximum likelihood angle and velocity estimation with space-time adaptive processing radar," in *Proc. Asilomar Conf. Signals, Syst. Comput.*, Pacific Grove, CA, USA, Nov. 1996, pp. 1265–1267, doi: 10.1109/ACSSC.1996.599148.
[23] W. L. Melvin, "A STAP overview," *IEEE Aerosp. Electron. Syst. Mag.*, vol. 19, no. 1, pp. 19–35, Jan. 2004.
[24] J. Capon, "High-resolution frequency-wavenumber spectrum analysis," *Proc. IEEE*, vol. 57, no. 8, pp. 1408–1418, Aug. 1969.
[25] M. Haardt and J. A. Nossek, "Simultaneous Schur decomposition of several nonsymmetric matrices to achieve automatic pairing in multidimensional harmonic retrieval problems," *IEEE Trans. Signal Process.*, vol. 46, no. 1, pp. 161–169, Jan. 1998.
[26] K. Sakaguchi, J. Takada, and K. Araki, "Multipath parameter estimation by using 3-D unitary ESPRIT," (in Japanese), IEICE, Tokyo, Japan, Tech. Rep. AP98-35, Jul. 1998, pp. 17–22.
[27] M. Haardt, C. Brunner, and J. Nossek, "Joint estimation of 2-D arrival angles, propagation delays, and Doppler frequencies in wireless communications," in *Proc. DSP Workshop*, Bryce Canyon, UT, USA, 1998, pp. 1–4.
[28] M. Haardt, F. Roemer, and G. D. Galdo, "Higher-order SVD-based subspace estimation to improve the parameter estimation accuracy in multidimensional harmonic retrieval problems," *IEEE Trans. Signal Process.*, vol. 56, no. 7, pp. 3198–3213, Jul. 2008.
[29] F. Raimondi, P. Comon, and O. Michel, "Wideband multilinear array processing through tensor decomposition," in *Proc. IEEE Int. Conf. Acoust., Speech Signal Process.*, Shanghai, China, Mar. 2016, pp. 2951–2955, doi: 10.1109/ICASSP.2016.7472218.
[30] S. Sahnoun, K. Usevich, and P. Comon, "Multidimensional ESPRIT for damped and undamped signals: Algorithm, computations, and perturbation analysis," *IEEE Trans. Signal Process.*, vol. 65, no. 22, pp. 5897–5910, Nov. 2017.
[31] F. Wen, C. Mao, and G. Zhang, "Direction finding in MIMO radar with large antenna arrays and nonorthogonal waveforms," *Digit. Signal Process.*, vol. 94, pp. 75–83, Nov. 2019, doi: 10.1016/j.dsp.2019.06.008.
[32] B. Ottersten, M. Viberg, and T. Kailath, "Performance analysis of the total least squares ESPRIT algorithm," *IEEE Trans. Signal Process.*, vol. 39, no. 5, pp. 1122–1135, May 1991.
[33] M. Wax and T. Kailath, "Detection of signals by information theoretic criteria," *IEEE Trans. Acoust., Speech, Signal Process.*, vol. 33, no. 2, pp. 387–392, Apr. 1985.
[34] M. Wax, "Detection and localization of multiple sources via the stochastic signals model," *IEEE Trans. Signal Process.*, vol. 39, no. 11, pp. 2450–2456, Nov. 1991.
[35] M. D. Zoltowski, M. Haardt, and C. P. Mathews, "Closed-form 2-D angle estimation with rectangular arrays in element space or beamspace via unitary ESPRIT," *IEEE Trans. Signal Process.*, vol. 44, no. 2, pp. 316–328, Feb. 1996.
[36] G. H. Golub and C. F. van Loan, *Matrix Computations*, 4th ed. Baltimore, MD, USA: TJHU Press, 2013.

KAZUSHI MORIMOTO received the B.E. degree in electrical and electronic engineering from Kyoto University, Kyoto, Japan, in 2017, and the M.E. degree in communications and computer engineering from the Graduate School of Informatics, Kyoto University, in 2019. He is currently with MaRI Company, Ltd., Kyoto. His research interest includes multidimensional adaptive signal processing for radar imaging.

TAKUYA SAKAMOTO (M'04–SM'17) received the B.E. degree in electrical and electronic engineering from Kyoto University, Kyoto, Japan, in 2000, and the M.E. and Ph.D. degrees in communications and computer engineering from the Graduate School of Informatics, Kyoto University, in 2002 and 2005, respectively.

From 2006 to 2015, he was an Assistant Professor with the Graduate School of Informatics, Kyoto University. From 2011 to 2013, he was a Visiting Researcher at the Delft University of Technology, Delft, The Netherlands. From 2015 to 2018, he was an Associate Professor with the Graduate School of Engineering, University of Hyogo, Himeji, Japan. In 2017, he was also a Visiting Scholar at the University of Hawaii at Manoa, Honolulu, HI, USA. Since 2018, he has been a PRESTO Researcher of the Japan Science and Technology Agency, Kawaguchi, Japan. He is currently an Associate Professor with the Graduate School of Engineering, Kyoto University. His current research interests are system theory, inverse problems, radar signal processing, radar imaging, and wireless sensing of vital signs.

Dr. Sakamoto was a recipient of the Best Paper Award from the International Symposium on Antennas and Propagation, in 2012, and the Masao Horiba Award, in 2016. In 2017, he was invited as a Semi-Plenary Speaker of the European Conference on Antennas and Propagation, Paris, France.

TORU SATO (M'92) received the B.E., M.E., and Ph.D. degrees in electrical engineering from Kyoto University, Kyoto, Japan, in 1976, 1978, and 1982, respectively. He has been with Kyoto University, since 1983, and is currently the Vice Director and Professor of the Institute for Liberal Arts and Sciences. His major research interests include system design and signal processing aspects of UWB radars, atmospheric radars, radar remote sensing of the atmosphere, and biomedical imaging. He is a Fellow of the Institute of Electronics, Information, and Communication Engineers of Japan, and a member of the Society of Geomagnetism and Earth, Planetary and Space Sciences, the Institute of Electrical Engineers of Japan, and the Institute of Electrical and Electronics Engineers.